Lasers in Manufacturing Conference 2017

Thermal & fluid field modelling for laser aided additive manufacturing

Youxiang Chew[a], Jie Song[a], Guijun Bi[a,*], Hui-Chi Chen[a], Xiling Yao[a], Baicheng Zhang[a], Jiaming Bai[a], Zhaoqin Guo[a] and Seung Ki Moon[b]

[a]*Singapore Institute of Manufacturing Technology, 73 Nanyang Drive, Singapore 637662*
[b]*School of Mechanical and Aerospace Engineering, Nanyang Technological University, 50 Nanyang Avenue, Singapore 639798*

Abstract

A numerical model is developed which integrates laser-powder interaction into overall heat flux input for computing the fully coupled melt-pool fluid and thermal field for clad geometries and transient thermal evolution predictions. Particle velocities and the focused powder jet diameter were measured experimentally and used for computing laser power attenuation effects under different powder feeding rates. This gives a more accurate modelling of the heat-flux incident upon the curved advancing melt-pool surface. The Marangoni effect will be considered to capture the enhanced convective heat transfer as well as the effects of melt-pool fluid flow on the clad bead profile. The clad bead shape is determined by the balancing of the external ambient pressure with the tangential and normal surface gradient. Mass addition into the melt-pool from the powder jets will be accounted for by using the moving mesh method, whereby the mesh velocity within the melt-pool is defined in accordance with local powder intensity distribution. The numerical results give good agreement when compared with experimentally obtained clad geometries & melt-pool depths under different laser power, laser scanning speed & powder feeding rates.

Keywords: Additive-Manufacturing ; Marangoni; Meltpool dynamics; laser cladding

1. Introduction

In laser aided additive manufacturing (LAAM) or laser metal deposition process, the physical phenomena involving the thermal and fluid fields will directly influence the solidification microstructure and

* Corresponding author. Tel.: +65-67938502
E-mail address: gjbi@simtech.a-star.edu.sg

subsequently the post-clad mechanical properties and performance (Thompson et al., 2015). The interaction between the thermal-fluid dynamics and powder jet dynamics will also inherently influence the clad bead and melt-pool dimensions. These microstructural and clad macro-characteristics of laser clad parts are important process outputs relevant to many applications across industries such as automobile, aerospace and gas & oil. Reliable numerical models capable of accurate clad dimension predictions are important to guide establishment of experimental process windows to meet the desired geometric specifications in LAAM applications. The thermal and fluid fields are also fundamental to further simulating the metallurgical and residual stress fields. The resultant metallurgical fields and residual stress distribution can then provide insights to understanding the correlation between process parameters with material mechanical performances. In addition, the melt-pool fluid flow and disturbances were found to have a major effect on the surface quality (Shah et al., 2010).

Numerical modelling with emphasis on melt-pool fluid flow (Kumar et al., 2009; Qi et al., 2006), residual stresses (Chew et al., 2015; Brückner et al., 2007), and dimensional accuracy (Y. S. Lee et al., 2016) have been reported by many researchers. 2D numerical model had demonstrated the multi-physics approach involving Marangoni flow to predict the clad and melt-pool sizes (Morville et al., 2012). The simulation of the powder particle flow fields have also been included to improve the heat-transfer simulation for solidification analysis (Nie et al., 2014). Numerical modelling of the fluid convection and melt-pool formation for Inconel 718 had been reported to yield good predictions of the melt-pool and clad geometry at lower laser power and powder feeing rate (Y. Lee et al., 2014). However, more research efforts are required to extent the applicability of these models under a wider range of process parameters and validated by actual experimental laser deposited clad beads.

For this purpose, the three-dimensional thermal and melt-pool fluid flow fields, tracking of the melt-pool moving surface and the associated mass and heat transfer from the powder stream will be included in the current numerical model. Powder feeding parameters such as the powder particle size, particle velocity and interaction between in-flight particles and laser irradiation, are incorporated in this model as these are known to further enhance the thermal-fluid model (Manvatkar et al., 2014). The powder catchment efficiency in this model was calculated from the melt-pool dynamics and powder feeding rate, instead of a predefined empirical value. In this numerical model, the effects of varying the main laser cladding process parameters on the thermal-fluid fields and clad dimensions will be investigated. The model for LAAM of Inconel 718 powder onto substrate of the same material is presented with experimental validation. The predicted clad bead dimensions will be presented along with illustrations of the melt pool shape, fluid flow velocity and temperature distribution.

The layout of the paper is as follows. In Section 2, the experimental procedure adopted in this study is introduced. In Section 3, the numerical model of the LAAM process using the FE software, COMSOL Multiphysics™ 5.2 is described. The comparison between experimental and numerical results and detailed discussion are conducted in Section 4. Section 5 ends the paper with conclusion and suggestions for future work.

2. Experiments

In this section, the experimental measurement of the powder particle velocity and powder jet diameter will be elaborated. The substrate laser absorptivity value of IN718 and the experimental clad bead dimensions and melt-pool depth will also be presented.

2.1. Powder jets

The laser power attenuation model requires the average particle velocity and the focused powder jet diameter at the standoff distance below the laser nozzle to compute the laser power attenuated and in-flight particle heating. These two parameters are determined experimentally. The powder particle jets are imaged at frame rate of 7500 frames per second to analyze the movement of particle clusters for velocity calculations. The imaged data analysis of 21 sets of powder cluster yields an average velocity of 8.3m/s with standard deviation of 1.48m/s. The powder stream diameter at the working plane where the powder jets converged into a powder focus is also estimated from image analysis. The focused powder stream diameter of 2.3mm is used to define the powder intensity distribution in the heat-flux equation. The measured substrate absorptivity after sandblasting corresponding to the laser wavelength of 1064nm is approximately 0.42. This laser absorptivity value is used in the numerical model.

2.2. LAAM experiments & numerical predictions.

LAAM experiments were performed to obtain the clad geometries and melt-pool depth for comparison with numerical results. The substrate was of length 60 mm, width 25 mm, and thickness 4 mm. The spot size of laser beam was 2.2 mm in diameter. The experiments, as shown in **Fehler! Verweisquelle konnte nicht gefunden werden.**, can be categorized into 3 sets according to the main process parameters varied within each set. The experiments numbered 1-3, 2, 4-5 and 2, 6-7, investigate the effects of varying laser power, powder feeding rate, and laser scanning speed on the clad and melt-pool dimensions. For experiments 2, 6-7 the powder feeding rate normalized by the scan speed is maintained constant, in order to better evaluate the effects of varying laser scanning speed. The IN718 powder particles were delivered by Argon carrier gas at a flow rate of 4l/min for the coaxial powder delivery system.

Table 1. Experimental parameters with experimental and predicted clad bead dimensions and melt-pool depths.

Expt. No.	Power (W)	Scan speed (mm/min)	Powder feeding rate (g/min)	Clad height (mm) Expt. / predicted	Clad wdith (mm) Expt. / predicted	Melt pool depth (mm) Expt. / predicted
1	640	600	4.35	0.516 / 0.554	2.000 / 1.876	0.571 / 0.630
2	840	600	4.35	0.511 / 0.561	2.175 / 2.015	0.981 / 0.891
3	1010	600	4.35	0.548 / 0.544	2.227 / 2.230	1.210 / 1.137
4	840	600	2.90	0.361 / 0.363	2.193 / 2.158	1.105 / 1.011
5	840	600	5.80	0.701 / 0.721	2.188 / 2.006	0.960 / 0.889
6	840	900	6.52	0.509 / 0.512	2.082 / 1.882	0.721 / 0.668
7	840	1200	8.70	0.511 / 0.558	1.951 / 1.784	0.459 / 0.436

3. Numerical model

In this section, the thermal and fluid boundary conditions will be presented. The details of the material properties utilized in the model will also be elaborated. The finite element software COMSOL Multiphysics™ 5.2 was employed to simulate the laser aided additive manufacturing process for deposition of a single clad bead of Inconel 718.

3.1. Thermal boundary conditions

The schematic of the finite element model is shown in Figure 1(a) below. The finite element model adopts a symmetric boundary condition at the plane located at clad bead center position, along the laser cladding direction. The thermal field of the half-bead model for experiment No. 2 is given in Figure 1(b) to illustrate the half-bead model. Convection and radiation boundary conditions were also applied on all the external boundaries.

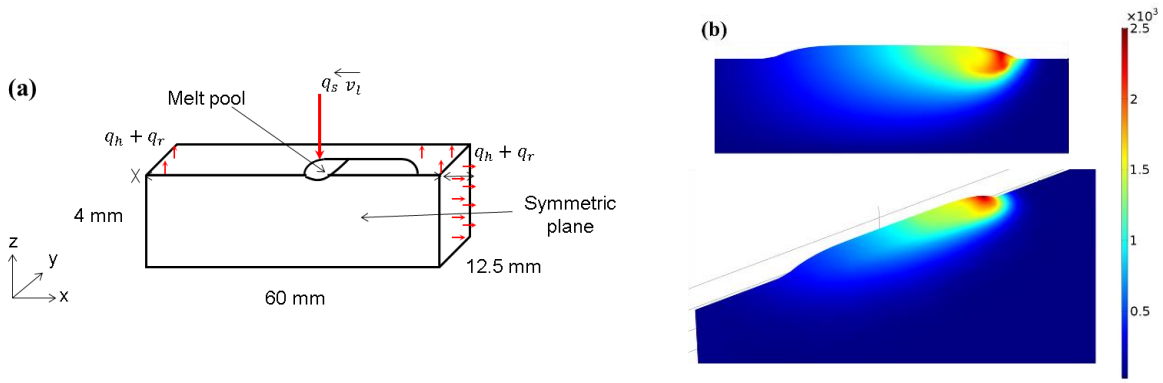

Fig. 1. Experimental set-up for deposition of single clad bead consisting of laser head, substrate and cooling plate.

The laser beam is represented as a Gaussian beam with spot radius R_l, laser powerP_l, and laser scanning speed of v_l. The powder intensity is assumed to follow the Gaussian distribution with radius R_p and feeding rate $\dot{m}$. The laser power attenuation model used in this work was enhanced from the methodology developed in the reference (Chew et al., 2015). In the laser power attenuation model, the applied net heat flux accounts for laser-particle jet interaction and attenuation effects. The overall heat-flux equation q_s applied on the substrate moving mesh surface domain is given as follows:

$$q_s = \alpha_s \left[\frac{2P_l}{\pi R_l^2} e^{-2\frac{r^2}{R_l^2}} - f(r) \right] cos\,\theta - \frac{2\dot{m}}{\pi R_p^2} e^{-2\frac{r^2}{R_p^2}} \left(L_f + c_{p,s}(T_m - T_i) + c_{p,l}(T - T_m) \right) Step(T)\, cos\,\theta \quad (1)$$

The overall heat flux equation consist of two main terms. These two main terms will be elaborated separately. The details for the derivation of $f(r)$ have been previously reported in (Chew et al., 2015) and not given here due to its length. The laser attenuation $f(r)$ term calculates the amount of laser power attenuated using parameters such as powder feeding rate, spatial distribution of the powder intensity, powder velocity and the powder jet diameter of 1mm at the inlet and expanding linearly to 2.3mm at the focused plane. The first term as expression (1.1) consists of the Gaussian laser beam and the laser power attenuation term $f(r)$. The cosθ term was included in both the first and second terms to consider the effective flux in the normal direction to the curved surface of the moving boundary. In which, θ is the angle between the surface normal of the substrate and the laser beam.

$$\textbf{\textit{First term}}: \alpha_s \left[\frac{2P_l}{\pi R_l^2} e^{-2\frac{r^2}{R_l^2}} - f(r) \right] cos\theta \qquad (1.1)$$

The second term accounts for the effect of powder particles entering the melt-pool with an initial temperature T_i. The particle initial temperature (just before melt-pool entry) caused by in-flight particle heating is computed using equation (2). From the calculated initial temperature T_i, the powder particles initial temperature were below the melting temperature T_m. Considering the relatively small size of the powder particle diameter (~30μm), it is assumed that the powder particles attain thermal equilibrium with the melt-pool surface almost immediately after entering the melt-pool. Hence, the Gaussian powder mass flux is considered as a heat sink source in the overall heat flux equation. The second term is given as:

$$\textbf{\textit{Second term}}: \frac{2\dot{m}}{\pi R_p^2} e^{-2\frac{r^2}{R_p^2}} \left(L_f + c_{p,s}(T_m - T_i) + c_{p,l}(T - T_m) \right) Step(T)\, cos\,\theta \qquad (1.2)$$

It should be noted that in equation (1.2), the latent heat of fusion for the powder particle is considered where $\boldsymbol{c_{p,s}}$ is the specific heat capacity at solidus temperature and $\boldsymbol{c_{p,l}}$ is the specific heat capacity at the liquidus temperature. The function $\boldsymbol{Step(T)}$ is included to consider only the effect of the powder mass flux incident within the melt-pool region. The details of the function $\boldsymbol{Step(T)}$ is given below.

$$Step(T) = \begin{cases} 1 & if\ T > T_m \\ 0 & if\ T < T_s \\ Smooth\ transition\ from\ 0\ to\ 1 & if\ T_s \leq T \leq T_m \end{cases} \qquad (2)$$

3.2. Fluid & moving mesh boundary conditions

The surface tension forces at the melt-pool surface comprises of the normal and tangential component. The normal component of the surface tension in equilibrium with the ambient pressure is the main factor affecting the clad bead shape. The tangential component drive the Marangoni fluid flow in the melt-pool. The force acting on the melt-pool surface is given below:

$$T \cdot n_m = \sigma \kappa n_m - \gamma \nabla_t T \qquad (3)$$

Whereby $\boldsymbol{T}$ is the stress tensor, $\boldsymbol{n_m}$ is the normal vector of the melt pool surface. The first term on the right-hand side corresponds to surface tension force, in which σ is the surface tension coefficient of the material and κ is the mean curvature of the melt pool surface. The second term corresponds to the Marangoni effect, in which γ is the thermocapillary coefficient (which is the temperature derivative of the surface tension coefficient) and ∇_t is the tangential derivative operator on the melt pool surface.

3.3. Material properties

The material properties of Inconel 718 used in the model are listed in Table 2. The thermal conductivity and specific heat capacity are temperature-dependent and can be found in the references (Sweet et al., 1987; Basak et al., 2003). More properties from the presented in Table 2 are obtained from (Mills, 2002;

Pottlacher et al., 2002; Metals, 2007). The laser absorptivity value is assumed to increase linearly from the measured experimental value at room temperature to 0.55 at melting temperature. The value 0.55 was estimated based on the temperature dependency of absorptivity values for IN718 reported in the reference (Sainte-Catherine et al., 1991). The surface tension values for IN718 were known to be affected by the presence of surface active elements such as sulfur and oxygen (P. D. Lee et al., 1998). The segregation and redistribution of theses surface active elements (Winkle et al., 2000) and interaction effects between the existing elements (McNallan et al., 1991) makes it difficult to determine an accurate analytical expression for temperature dependent surface tension coefficient. Hence, in this study a positive surface tension coefficient gradient is assumed (Y. S. Lee & Farson, 2016), and the values of γ is calibrated using experiment No. 1 and subsequently applied to predict all the cases.

Table 2. Material properties of Inconel 718 used in the finite element model

Property	Value
Density, ρ	$8193.3\ \mathrm{kg/m^3}$
Thermal conductivity, k	Temperature-dependent, 11.1~28.3 $\mathrm{W/(m \cdot K)}$
Specific heat capacity, c_p	Temperature-dependent, 460.0~894.8 $\mathrm{J/(kg \cdot K)}$
Sintering temperature, T_s	1260 ℃
Melting temperature, T_m	1336 ℃
Latent heat, L_f	227 kJ/kg
Viscosity, μ	$0.196e^{5848/T}$ mPa
Surface tension coefficient at T_m, σ_0	$1.6\ \mathrm{N/m}$
Thermo-capillary gradient, γ	$5.4 \times 10^{-5}\ \mathrm{N/(m \cdot K)}$
Thermal expansion coefficient, α	$1.4 \times 10^{-5}\ 1/\mathrm{K}$

4. Results and discussion

The dimensions of the clad height, width and melt-pool depth presented in Table 1 show good agreement between experimental and numerical results. A maximum difference of 10% is observed for the melt-pool depth of case 1 where the model slightly over-predicts the depth. Hence, the developed numerical model has shown to give reasonably good geometric predictions. The predicted fluid and thermal field for experiment No. 4 is given in Figure 2(a) and 6(b) below. Figure 6(a) shows the transverse cross-section of the clad bead, whereby the fluid flows from the melt-pool edge towards the melt-pool center at the surface, going down subsequently to the deepest section before returning to the edge to form a vortex structure. This fluid flow direction brings the molten fluid with the highest temperature from the surface down to the bottom, resulting in a narrower but deeper melt-pool profile. Outside the thermal contour line of 1936 ℃, the fluid velocity decreases until the contour line for T_m whereby heat-conduction becomes the dominant heat transfer mode.

In Figure 2(b), the clad bead longitudinal cross-section in the laser clad direction is shown. Two vortices can be observed with the smaller vortex located at the melt-pool leading edge. The highest fluid velocity is located beneath the region with highest melt-pool temperature. For the second trailing edge vortex, the fluid flow direction is from the melt-pool trailing edge towards the laser beam centre location before going down towards the melt-pool depth direction. At the melt-pool bottom region, the fluid flow direction is almost horizontal near the deepest point of the melt-pool. Thereafter, the fluid flow direction gradually turn upwards towards the increasingly shallower regions till the melt-pool trailing edge before continuing on the recirculation path back to the laser beam centre location. When comparing the flow field of experiment No 7. (melt-pool depth=0.46mm) with experiment No 4. (melt-pool depth=1.1mm), it was observed that the deeper melt-pool also has a higher downwards fluid velocity component. For instance in the clad bead

longitudinal view, the velocity in the downward direction is 0.31m/s and 0.43m/s for experiment No. 7 and No. 4 respectively.

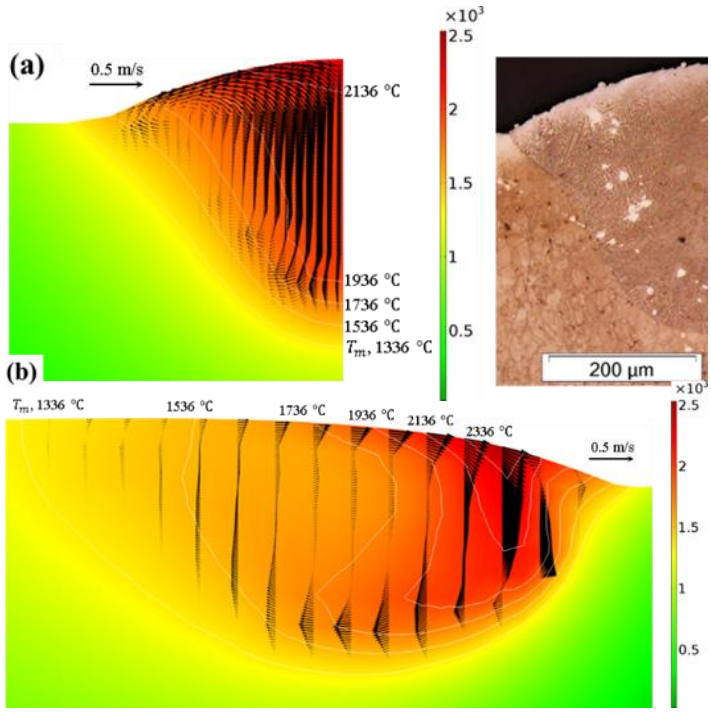

Fig. 2. (a) Melt-pool thermal and fluid fields for exp. No. 4 in the clad bead transverse cross-sectional view and; (b) in the clad bead longitudinal cross-sectional view along the cladding direction.

5. Conclusions and future work

The developed numerical model were able to predict the clad bead and melt-pool dimensions within 10% based on experimental results under the following LAAM conditions: laser power in the range of 640W to 1010W, laser scanning speed from 300mm/s to 1200mm/s and powder feeding rate from 2.9g/min to 8.7g/min. One of the key feature of the numerical model is the application of the moving mesh (ALE) domain to simulate the physical boundary of the three-dimensional melt-pool surface for convenient application of thermal boundary heat flux, powder feeding mass flux and moving mesh velocity boundary conditions in the normal direction. The combination of these applied boundary conditions were able correctly predict the clad height without the need to specify a predefined powder catchment efficiency. For future work, the model can be further extended for investigating the dimensional accuracies of multiple overlapping clad beads or multiple-layered single bead wall. The simulated thermal and fluid fields can also be used as boundary conditions for further prediction of the metallurgical field. An additional concentration field can also be added to the thermal and fluid field to study the convective mass transport and mixing of different alloying elements.

Acknowledgements

The authors wish to acknowledge the support from A*STAR SERC for funding the Laser-aided Additive Manufacturing (Work Package 1) for this research work.

References

Thompson, S. M., Bian, L., Shamsaei, N., & Yadollahi, A. (2015). An overview of Direct Laser Deposition for additive manufacturing; Part I: Transport phenomena, modeling and diagnostics. *Additive Manufacturing, 8*, 36-62. doi: http://doi.org/10.1016/j.addma.2015.07.001

Shah, K., Pinkerton, A. J., Salman, A., & Li, L. (2010). Effects of Melt Pool Variables and Process Parameters in Laser Direct Metal Deposition of Aerospace Alloys. *Materials and Manufacturing Processes, 25*(12), 1372-1380. doi: 10.1080/10426914.2010.480999

Kumar, A., & Roy, S. (2009). Effect of three-dimensional melt pool convection on process characteristics during laser cladding. *Computational Materials Science, 46*(2), 495-506. doi: https://doi.org/10.1016/j.commatsci.2009.04.002

Qi, H., Mazumder, J., & Ki, H. (2006). Numerical simulation of heat transfer and fluid flow in coaxial laser cladding process for direct metal deposition. *Journal of Applied Physics, 100*(2), 024903. doi: 10.1063/1.2209807

Chew, Y., Pang, J. H. L., Bi, G., & Song, B. (2015). Thermo-mechanical model for simulating laser cladding induced residual stresses with single and multiple clad beads. *Journal of Materials Processing Technology, 224*, 89-101. doi: https://doi.org/10.1016/j.jmatprotec.2015.04.031

Brückner, F., Lepski, D., & Beyer, E. (2007). Modeling the Influence of Process Parameters and Additional Heat Sources on Residual Stresses in Laser Cladding. *Journal of Thermal Spray Technology, 16*(3), 355-373. doi: 10.1007/s11666-007-9026-7

Lee, Y. S., & Farson, D. F. (2016). Surface tension-powered build dimension control in laser additive manufacturing process. *The International Journal of Advanced Manufacturing Technology, 85*(5), 1035-1044. doi: 10.1007/s00170-015-7974-5

Morville, S., Carin, M., Peyre, P., Gharbi, M., Carron, D., Masson, P. L., & Fabbro, R. (2012). 2D longitudinal modeling of heat transfer and fluid flow during multilayered direct laser metal deposition process. *Journal of Laser Applications, 24*(3), 032008. doi: 10.2351/1.4726445

Nie, P., Ojo, O. A., & Li, Z. (2014). Modeling analysis of laser cladding of a nickel-based superalloy. *Surface and Coatings Technology, 258*, 1048-1059. doi: https://doi.org/10.1016/j.surfcoat.2014.07.030

Lee, Y., Nordin, M., Babu, S., & Farson, D. (2014). Influence of fluid convection on weld pool formation in laser cladding. *Welding Journal, 93*(8), 292S-300S.

Manvatkar, V., De, A., & DebRoy, T. (2014). Heat transfer and material flow during laser assisted multi-layer additive manufacturing. *Journal of Applied Physics, 116*(12), 124905. doi: 10.1063/1.4896751

Sweet, J. N., Roth, E. P., & Moss, M. (1987). Thermal conductivity of Inconel 718 and 304 stainless steel. *International Journal of Thermophysics, 8*(5), 593-606. doi: 10.1007/bf00503645

Basak, D., Overfelt, R. A., & Wang, D. (2003). Measurement of Specific Heat Capacity and Electrical Resistivity of Industrial Alloys Using Pulse Heating Techniques. *International Journal of Thermophysics, 24*(6), 1721-1733. doi: 10.1023/b:ijot.0000004101.88449.86

Mills, K. C. (2002). Ni - IN 718 *Recommended Values of Thermophysical Properties for Selected Commercial Alloys* (pp. 181-190): Woodhead Publishing.

Pottlacher, G., Hosaeus, H., Kaschnitz, E., & Seifter, A. (2002). Thermophysical properties of solid and liquidInconel 718 Alloy*. *Scandinavian Journal of Metallurgy, 31*(3), 161-168. doi: 10.1034/j.1600-0692.2002.310301.x

Metals, S. (2007). Inconel alloy 718. *Publication Number SMC-045. Special Metals Corporation*.

Sainte-Catherine, C., Jeandin, M., Kechemair, D., Ricaud, J.-P., & Sabatier, L. (1991). Study of dynamic absorptivity at 10.6 µm (CO2) and 1.06 µm (Nd-YAG) wavelengths as a function of temperature. *J. Phys. IV France, 01*(C7), C7-151-C157-157.

Lee, P. D., Quested, P. N., & Mclean, M. (1998). Modelling of Marangoni effects in electron beam melting. *Philosophical Transactions of the Royal Society of London. Series A: Mathematical, Physical and Engineering Sciences, 356*(1739), 1027-1043. doi: 10.1098/rsta.1998.0207

Winkle, C., Amberg, G., Inoue, H., Koseki, T., & Fuji, M. (2000). Effect of surfactant redistribution on weld pool shape during gas tungsten arc welding. *Science and Technology of Welding and Joining, 5*(1), 8-20. doi: 10.1179/stw.2000.5.1.8

McNallan, M. J., & Debroy, T. (1991). Effect of temperature and composition on surface tension in Fe-Ni-Cr alloys containing sulfur. *Metallurgical Transactions B, 22*(4), 557-560. doi: 10.1007/bf02654294